LASER & PHOTONICS REVIEWS
www.lpr-journal.org

Ultralow Photon Flux OWC Links Using UV-C Single-Photon Detection

Feng Liu, James Farmer, Grahame Faulkner, Jonathan J. D. McKendry, Enyuan Xie, Qianfang Zheng, Zhaoming Wang, Jianming Wang, Jordan Hill, Johannes Herrnsdorf, Martin D. Dawson, and Dominic O'Brien**

Low photon flux optical wireless communication (OWC) links are difficult to operate under normal daylight conditions as the interference from daylight will overwhelm any signal. However, in the UV-C region of the spectrum, light from the sun is highly attenuated, offering the possibility of link operation. In this paper, ultralow photon flux OWC links using a UV-C micro-LED and a silicon photomultiplier (SiPM) based UV-C single-photon detector (SPD) are reported. A 1 megabaud per second (MB s^{-1}) symbol rate 128-pulse-position modulation (128-PPM) link is demonstrated with 7.7 transmitted photons per bit, corresponding to 0.97 detected photon per bit. A maximum bit rate of 120 Mbit s^{-1} is achieved in 8-PPM links with a transmitted power of 1.7 nW. In addition, a 500 MHz single-photon link is established with a bit error rate (BER) of 4.32×10^{-2} and a measured bit rate of 2.12 Mbit s^{-1}, showing the potential for a quantum key distribution (QKD) system operating at the UV-C region.

1. Introduction

Optical wireless communication (OWC) is a critical technology poised to provide terminal wireless access services in future wireless communication systems because of its broad bandwidth, low latency, anti-electromagnetic interference and no regulatory requirements.[1,2] In addition to pursuing a high data rate,[3,4] achieving ultralow photon flux is another key topic in OWC research.[5–9] For instance, quantum key distribution (QKD), which can generate secure keys with absolute confidentiality based on the no-cloning theorem, has attracted widespread attention.[7–9] To establish ultralow photon flux OWC links for both indoor and outdoor applications, mitigating sunlight interference is a crucial consideration.[10] This is because the signal power is extremely low, typically at the pW level, and even very limited sunlight interference can destroy the links. In the sunlight spectrum, there exists a solar-blind region within the UV-C band, covering 200 to 280 nm. The sunlight radiation of this region reaching the earth's ground is extremely low, less than 5×10^{-23} W (m^2 nm) − 1, compared with over 0.8 W (m^2 nm) − 1 sunlight radiation in the visible band.[11] However, despite the advantages of interference, UV-C light is extremely harmful to human eyes and body. According to the eye and skin safety standards, the exempt level of UV solar-blind light is only 1 mW m^{-2}.[12] Exempt links are feasible at the low photon fluxes considered here, but they are highly constrained by these considerations.

Single-photon detectors (SPD) are devices which possess high sensitivity and a low dark count rate (DCR), playing a crucial role in ultralow photon flux links. To create such detectors in the UV-C band, several materials are promising candidates, including molybdenum silicide (MoSi), silicon carbon (SiC), gallium nitride (GaN) and silicon (Si).[13–18] A reported MoSi superconducting nanowire single-photon detector (SNSPD) has a photon detection efficiency (PDE) exceeding 70% and a DCR of approximately 0.25 count per second (cps) but is limited due to the low operating temperature of 4 K.[15] In the case of SiC and GaN single-photon avalanche diodes (SPAD), the DCR is over 1 Mcps mm^{-2} at room temperature with a PDE of approximately 10%.[16] Among all Si-based photodetectors, the silicon photomultiplier (SiPM) is specifically designed for photon counting. Compared with the above three materials, a SiPM has a low DCR (≈50 kcps mm^{-2}), a large active area (≥1 mm^2) and a suitable

F. Liu, J. Farmer, G. Faulkner, Z. Wang, J. Wang, D. O'Brien
Department of Engineering Science
University of Oxford
Parks Road, Oxford OX1 3PJ, UK
E-mail: feng.liu@eng.ox.ac.uk; dominic.obrien@eng.ox.ac.uk

J. J. D. McKendry, E. Xie, J. Hill, J. Herrnsdorf, M. D. Dawson
Institute of Photonics
Department of Physics
SUPA
University of Strathclyde
Glasgow G1 1RD, UK

Q. Zheng
Department of Materials
University of Oxford
Parks Road, Oxford OX1 3PH, UK

The ORCID identification number(s) for the author(s) of this article can be found under https://doi.org/10.1002/lpor.202401804

DOI: 10.1002/lpor.202401804

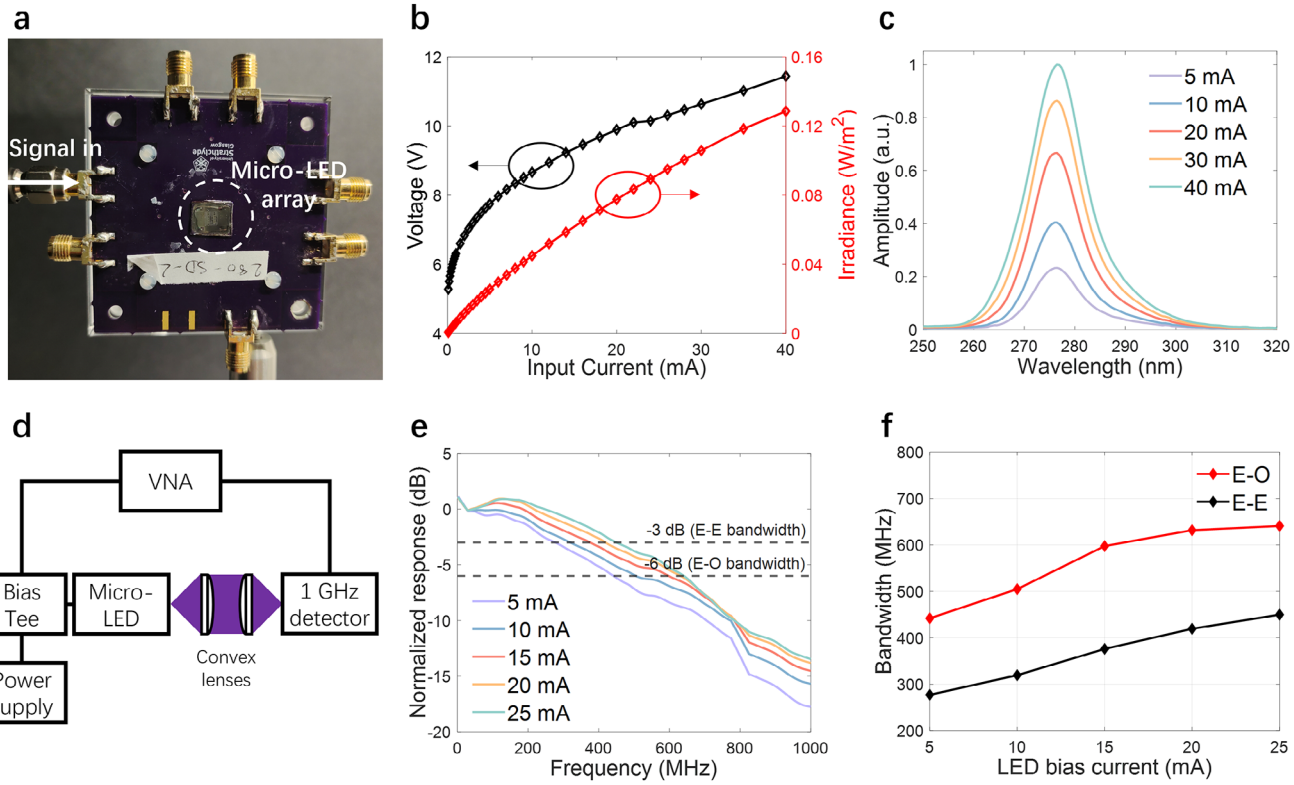

Figure 1. Characterizations of the 100 μm UV-C micro-LED. a) UV-C micro-LED array image. b) *I–V–I* curves at 6.5 cm distance. c) Spectrum under different driving current. d) Block diagram of the experiment measuring the 3-dB bandwidth. e) Normalized response versus frequency with bias current ranging from 5 to 25 mA. f) Measured E–E and E–O bandwidth versus LED bias current.

PDE (≈15%) for UV solar-blind light at room temperature.[19] The use of SiPMs has been investigated in multiple applications, such as OWC, biophotonics and LiDAR.[20–23] For OWC systems, more than 1 Gbit s^{-1} OWC links have been demonstrated with SiPM.[20,21]

In addition to the SPD, a high-speed transmitter is another significant element for building high data rate UV-C ultralow photon flux links. Due to the lack of a commercial UV-C laser diode and the low speed of commercial UV-C LEDs (typical bandwidth ≤10 MHz), the micro-LED is a potential solution because of its high modulation bandwidth.[24–27] The micro-LED's modulation bandwidth increases with decreasing diameter and micro-LEDs with different diameters are suited to different applications.[27] Smaller micro-LEDs offer higher modulation speeds and pixel density, making them ideal for high-speed optical communications and displays.[28–30] In contrast, larger micro-LEDs provide higher optical power, making them more suitable for illumination applications.[31] Micro-LEDs can emit at a range of wavelengths.[32] In the UV-C region, AlGaN micro-LEDs with a diameter of around 100 μm have been reported.[26,27] They exhibit a peak wavelength of ≤280 nm, an output power of ≤1 mW, and a large bandwidth exceeding 100 MHz. Over 1 Gbit s^{-1} OWC links using UV-C micro-LEDs have been reported and the maximum transmission distance has reached 100 m.[33–35]

In this paper, a SiPM-based UV-C SPD is reported. Based on this SPD and a UV-C micro-LED, a minimum transmitted photon number per bit of 7.7 (corresponding to 0.97 detected photon per bit) was demonstrated in 1 Mb s^{-1} 128-pulse-position modulation (128-PPM) links and a maximum data rate of 120 Mbit s^{-1} was achieved in 40 Mb s^{-1} 8-PPM links. Additionally, a single-photon link was established with a measured bit error rate (BER) of 4.32×10^{-2}, showing the potential for building a wireless UV-C QKD system.

The remainder of this paper is organized as follows. In the Results section, the micro-LED characterization, UV-C SPD design and UV-C SPD characterization are presented in turn. Then, the experimental setup for ultralow photon flux links is introduced, followed by the performance of PPM links and single-photon links. The Discussion section examines the results, and the Experimental section explains the techniques employed, including micro-LED design and manufacture, PCB design and differentiation scheme.

2. Results and Discussion

2.1. Micro-LED Characterization

The light source of this work is a micro-LED array comprising three different diameters of micro-LEDs (100, 200, and 300 μm) of which an image can be seen of the assembly as shown in **Figure 1a**. The three micro-LEDs are bonded at the central region of the PCB, with each micro-LED being connected to an external mounted SMA port. These micro-LEDs are manufactured based on AlGaN at the Institute of Photonics, Department of Physics,

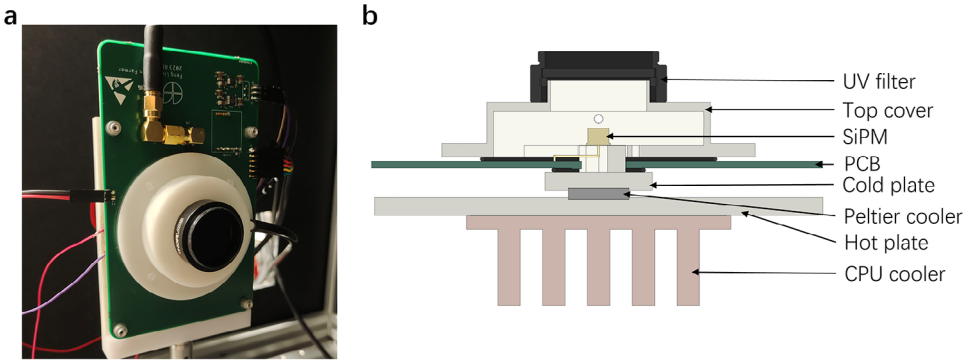

Figure 2. UV-C SPD design. a) UV-C SPD photography. b) Section view.

SUPA, University of Strathclyde.[26] To pursue the highest data rate, the 100 μm micro-LED is selected because the micro-LED's modulation bandwidth increases with decreasing diameter. The micro-LED was driven by a source meter unit (KEITHLEY 2636B) and the irradiance was measured by a power meter (Newport 843-R with a UV-enhanced Si head 818 UV/DB) at a distance of 6.5 cm. A plot of the micro-LED's voltage and irradiance versus current (*I–V–I* curves) is shown in Figure 1b. This shows the turn-on voltage is approximately 5 V. By using a spectrometer (Ocean Insight OFX00951), the spectrum of the micro-LED versus wavelength with driving current varying from 5 mA to 40 mA was measured and illustrated in Figure 1c. The spectrum covers both parts of the UV-B and UV-C regions and the full width at half maximum (FWHM) is approximately 11 nm. The emitted peak wavelength is 276 nm.

A block diagram of the experiment measuring the micro-LED's 3-dB bandwidth is shown in Figure 1d. AC signals (sine wave) generated by a vector network analyzer (VNA, Agilent Technologies FieldFox N9923A) and DC bias provided by a power supply (ROHDE & SCHWARZ HMP4040) are combined by a Bias Tee (Mini-Circuits ZFBT-6GW) and then forwarded to the micro-LED. Two UV convex lenses (Thorlabs LA4052-UV) collimate light from the micro-LED and focus light to the active area of a 1 GHz detector (HAMAMATSU C5658 APD module), respectively. Subsequently, the detector forwards the signal to the VNA, and the 3 dB bandwidth is obtained by sweeping the S21 value versus frequency. Figure 1e shows the normalized response of the VNA's S21 value with the micro-LED bias current ranging from 5 to 25 mA. The electrical-to-electrical (E-E) or electrical-to-optical (E-O) bandwidth is defined as the frequency at which there is a 3 dB attenuation of electrical power or optical power. Because the VNA measures electrical power loss of VNA-optical-VNA, the -3 dB and -6 dB attenuations of the normalized response correspond to the E-E and E-O bandwidth, respectively. The E-E and E-O bandwidth values are shown in Figure 1f. The result shows that as the bias current increases from 5 to 25 mA, the E-E bandwidth expands from 277 MHz to 450 MHz, and the E-O bandwidth increases from 442 to 641 MHz.

2.2. UV-C SPD Design

A UV-sensitive SiPM (HAMAMATSU S13360-1350 SPL) with 1.3 mm × 1.3 mm active area is chosen as the photodetector. A SiPM has an array of pixels with a SPAD in each. Every SPAD can be independently fired by a detected photon or a dark count, generating a single pulse corresponding to either a photon pulse or a dark pulse. However, according to the datasheet, the DCR of the UV-sensitive SiPM is extremely high (≈90 kcps) for establishing single-photon links.[36] Thus, the key for establishing such a link is to reduce the SiPM's DCR and one effective method is to reduce the operating temperature.[5,19] The image and section view of the UV-C SPD are shown in **Figure 2**a,b, respectively.

For the cooling design, the central component is a Peltier cooler (OTX20-68-F1A-1313-11-W2.25). On the cold side, a cold plate goes through the PCB, establishing a thermal connection between the SiPM and the Peltier cooler. The cold plate is fabricated from ceramic aluminum oxide because of its high thermal conductivity (≈30 W m^{-1} K^{-1}) and effective electrical isolation. Because the temperature will be reduced to below 0 °C, and to prevent freezing condensation, a plastic top cover and a UV filter (Thorlabs FGUV5 M) are used to create a confined space around the SiPM. A vacuum pump (RS vacuum pump) is then used to evacuate the air from the confined space. On the hot side, the heat flows to a liquid CPU cooler (MASTER LIQUID LITE 240) through the hot plate, which is also made of aluminum oxide. To achieve temperature control, a NTC thermistor (TDK B57540G1103F005) is placed on the cold plate close to the SiPM and a TEC controller (Meerstetter Engineering TEC-1161-4A) drives the Peltier cooler dynamically to control the temperature of the SiPM.

2.3. UV-C SPD Characterization

Figure 3a shows the dark current of the SiPM changing with bias voltage and temperature. The PCB and TEC controller are remotely controlled by a laptop to change the bias voltage and temperature, respectively. The dark current is measured by the source meter (KEITHLEY 2636B). The result shows a decrease in dark current with the reduction of temperature and bias voltage. The red curve (also in Figure 3b) presents the dark current versus temperature under the recommended bias voltage. The breakdown voltage of the SiPM decreases with temperature, and the PDE and gain depend on the overvoltage (bias voltage = breakdown voltage + overvoltage). To maintain unchanged PDE and gain by fixing the overvoltage, the recommended bias voltage decreases from 54.34 to 51.91 V with temperature varying from 25 °C to −20 °C,

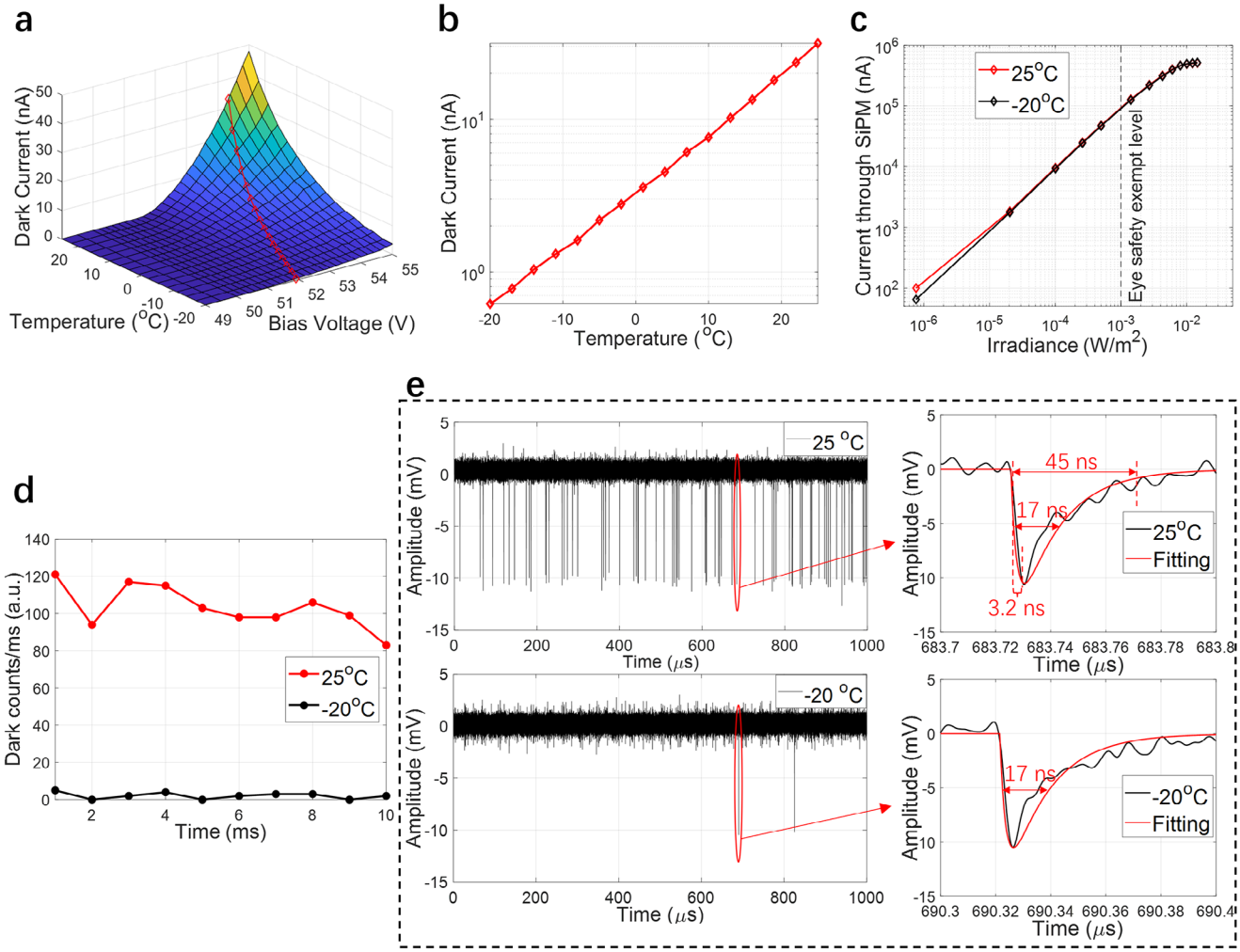

Figure 3. Characterizations of the UV-C SPD. a) Dark current versus bias voltage and temperature. b) Dark current versus temperature under recommended bias voltages. c) Current through the SiPM versus irradiance from the micro-LED. d) Dark counts versus time. e) Dark pulses during 1 ms period and zoomed-in single pulses under 25 °C and –20 °C.

according to the breakdown voltage change of 54 mV °C^{-1}. The result shows an approximately 11 dB reduction in dark current with a 30 °C cooling, consistent with the reported result.[19] The dark current at 25 °C and −20 °C are 29.08 nA and 0.57 nA, respectively. Further reducing the temperature is challenging, limited by the capability of the Peltier cooler, CPU cooler and SiPM construction. Note that the SiPM is always driven at the recommended bias voltage under different temperatures in the rest of the paper.

The current through the SiPM (photocurrent + dark current) at both 25 °C and −20 °C, varying with irradiance from the micro-LED is shown in Figure 3c. The power meter measures the irradiance from the micro-LED and then is replaced by the UV-C SPD at the same position with current measured by the source meter. It can be found that the two curves overlap each other well indicating that the PDE and gain remain constant under both 25 °C and −20 °C. The current difference at very low irradiance is because of the different dark current under different temperatures. The SiPM approaches saturation when the irradiance exceeds 10 mW m^{-2}, corresponding to an incident power of 17 nW.

To measure the DCR, the output from the SiPM of dark pulses is captured by an oscilloscope (AGILENT MSO6104A) and post-processed offline. The number of dark counts per ms over a 10 ms period is shown in Figure 3d. The DCR at 25 °C and −20 °C are calculated as 103.4 kcps and 2.1 kcps, respectively. Considering the dark current values in Figure 3b, the gain of the SiPM is calculated by:

$$G = \frac{I_d}{\mathrm{DCR} \cdot e_0} \tag{1}$$

where I_d and e_0 are the dark current and the elementary charge. Thus, the gain is 1.76×10^6 and 1.7×10^6 at 25 °C and −20 °C, respectively. The PDE can be obtained by:

$$\mathrm{PDE} = \frac{\left(I_t - I_d\right) \cdot h \cdot c}{G \cdot e_0 \cdot E_e \cdot A \cdot \lambda} \tag{2}$$

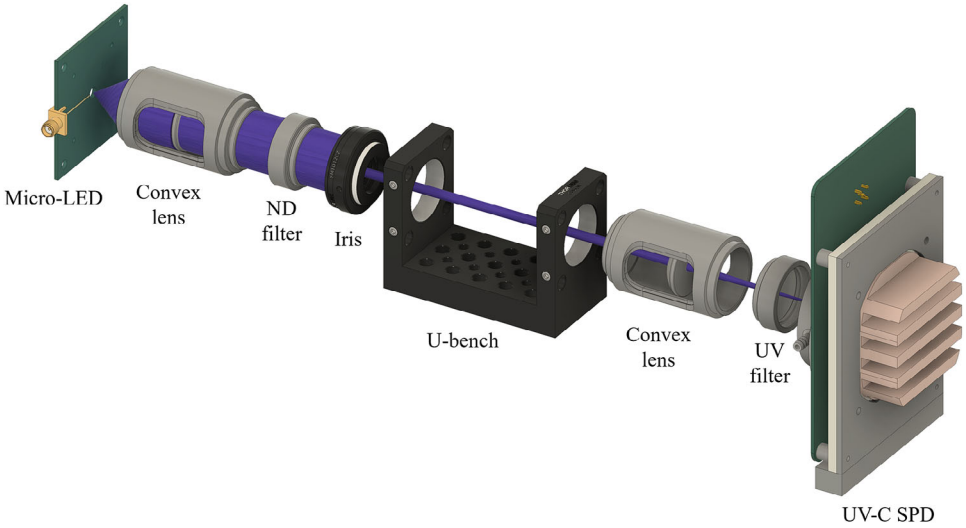

Figure 4. Experiment setup for ultralow photon flux links.

where I_t is the total current flowing through the SiPM and E_e is the irradiance. h and c are Planck's constant and the speed of light, respectively. A is the active area of the SiPM and λ is the wavelength. Thus, the PDE is calculated as 14.24% and 14.76% at 25 °C and −20 °C.

The captured dark pulses at 25 °C and −20 °C are plotted in Figure 3e. It can be seen that the pulses can clearly be distinguished from the noise floor. The left two diagrams represent dark pulses within a 1 ms period, showing a significant reduction in the number of dark counts with cooling. The right two diagrams illustrate two zoomed-in single pulses at 25 °C and −20 °C, respectively. The figures show exponential curves fitted to the data, following the form of:[37]

$$A_f\ (t) = A_0 \cdot \left(e^{-\frac{t}{T_r}} - e^{-\frac{t}{T_f}} \right) \tag{3}$$

where A_0 is the amplitude of the single pulse. T_r and T_f are the rise time and fall time of the single pulse, respectively. Both pulses show a peak amplitude of approximately 10.5 mV, with rise times (from 10% to 90% peak amplitude) measured at 3.2 ns. Thus, the practical 3-dB bandwidth of the UV-C SPD is estimated at 110 MHz, assuming that Bandwidth ≈ 0.35/rise time. The FWHM of the single pulse is measured as 17 ns. The dead time of each pixel is measured as 45 ns, with the dominant contributor being the fall time, constrained by the SiPM itself. Note that during the dead time, the pixel is rendered inactive but other pixels in the array can be fired by detected photons or dark counts.

2.4. Experimental Setup for Ultralow Photon Flux Links

The experimental setup for ultralow photon flux links is shown in **Figure 4**. At the transmitter, an arbitrary waveform generator (AWG, Tektronix AWG70002A) generates a modulated signal, and the source meter supplies a DC bias, which are combined by a Bias Tee (Mini-Circuits ZFBT-6GW) and then routed to the micro-LED. A convex lens is placed in a slotted tube (Thorlabs SM1L20C) for collimating the light emitted from the micro-LED. An ND filter (Thorlabs NDUV30A) and an iris (Thorlabs SM1D12CZ) are employed to attenuate the optical power to a specific value. The diameter of the light beam is constrained to 6 mm by the iris for the experiment represented here. A U-bench (Thorlabs CBB1/M) connects the transmitter and the receiver for precise alignment. At the receiver, a convex lens focuses the collimated light onto the active area of the SiPM. A UV filter in front of the receiver permits only UV light to enter, with an optical density of 2 (OD2) for visible light and OD1 for IR light. The received power at the SPD can be calculated as:

$$P_{\mathrm{RX}} = P_{\mathrm{TX}} \cdot T_{\mathrm{c}} \cdot T_{\mathrm{f}} \tag{4}$$

where P_{TX} is the transmitted power. T_{c} and T_{f} are the transmission of the convex lens and UV filter, which are measured as 92.4% and 83.0%, respectively. The temperature of the SiPM is maintained at −20 °C by the TEC controller. The received pulses displayed on the oscilloscope were captured for post-processing. More details on the experimental setup can be found in Note S1 (Supporting Information).

2.5. PPM Link Performance

The PPM scheme encodes information by transmitting a pulse in one of the multiple time slots during one symbol period. Using M-PPM as an example, one symbol period is equally divided into M time slots, so $\log_2$M bits can be encoded into one symbol. Previous research has demonstrated that the PPM scheme is an effective approach for minimizing power consumption, a critical factor in building deep-space and underwater optical communication systems.[38–42]

During our PPM links demonstration, in the transmitter, the pseudorandom binary sequence (PRBS) was modulated into a PPM sequence and transmitted by the micro-LED. Take 8-PPM as an example, "000" in the PRBS sequence is encoded as "10 000 000" in the PPM sequence, so the micro-LED emits light

Table 1. Transmitter settings of PPM links.

Symbol rate (Mb s^{-1})	0.1	0.2	0.5	1	2	3	2	5	10	20	40	50
PPM index *M*	128	128	128	128	128	128	8	8	8	8	8	8
Bit rate (Mbit s^{-1})	0.7	1.4	3.5	7	14	21	6	15	30	60	120	150
Transmitted photons per bit	8.6	8.6	8.6	8.6	8.6	8.6	20	20	20	20	20	20
Transmitted power (pW)	4.32	8.64	21.6	43.2	86.4	129.6	86.4	216	432	864	1728	2160

at the first time slot. The pulse width was set as 2 ns, considering the measured micro-LED's E-O bandwidth of around 500 MHz.

With the average transmitted photon number per symbol of 60 and symbol rate varying from 100 kb s^{-1} to 50 Mb s^{-1}, the corresponding PPM index *M*, bit rate, transmitted photons per bit and transmitted power are shown in **Table 1**. Considering the maximum transmitted power of 2.16 nW and 6 mm beam diameter, the transmitted irradiance is calculated as 76 μW m^{-2}, less than the safety exempt level 1 mW m^{-2}. Moreover, to explore the sensitivity limit of the UV-C SPD, the average transmitted photon number per symbol was changed from 40 to 70 at 128-PPM links with the symbol rate of 1 Mb s^{-1} (corresponding transmitted power from 28.8 to 50.4 pW).

In the receiver, a cascaded post-processing (CPP) scheme, including a differentiation scheme, data summing and decision, was applied, which is shown in **Figure 5**a. First, the received pulses were synchronized to the transmitted PPM sequence by correlation and the differential scheme is applied to mitigate the inter-symbol interference (ISI) due to the long fall time of pulses.[43] Second, the detection window was set as 2 ns to match the pulse width in the transmitter and the points within each detection window were summed respectively. Thirdly, the symbols decision was achieved by finding the minimum summed value among *M* detection windows within each symbol, followed by calculating symbol error rate (SER) and BER.

To prove the superiority of our CPP, SER and BER without the CPP were also considered. The decision was directly carried out by finding the minimum value from the original received pulses instead of the minimum summed value. Based on the Poisson distribution, the standard quantum limit for PPM is 5 detected photons per symbol for a BER of 3.8×10^{-3}.[44] The value 3.8×10^{-3} is the forward error correction (FEC) threshold for BER at which error-free can be achieved with a 7% overhead.[26] In this PPM link demonstration, considering the convex lens' transmission, UV filter's transmission and SiPM's PDE, the 60 transmitted photons per symbol correspond to 6.8 detected photons per symbol (corresponding to 0.97 detected photon per bit), which is close to the standard quantum limit.

Each point of BER or SER was calculated based on $100 \times 2^7 = 12800$ symbols. The calculated SER and BER versus symbol rate

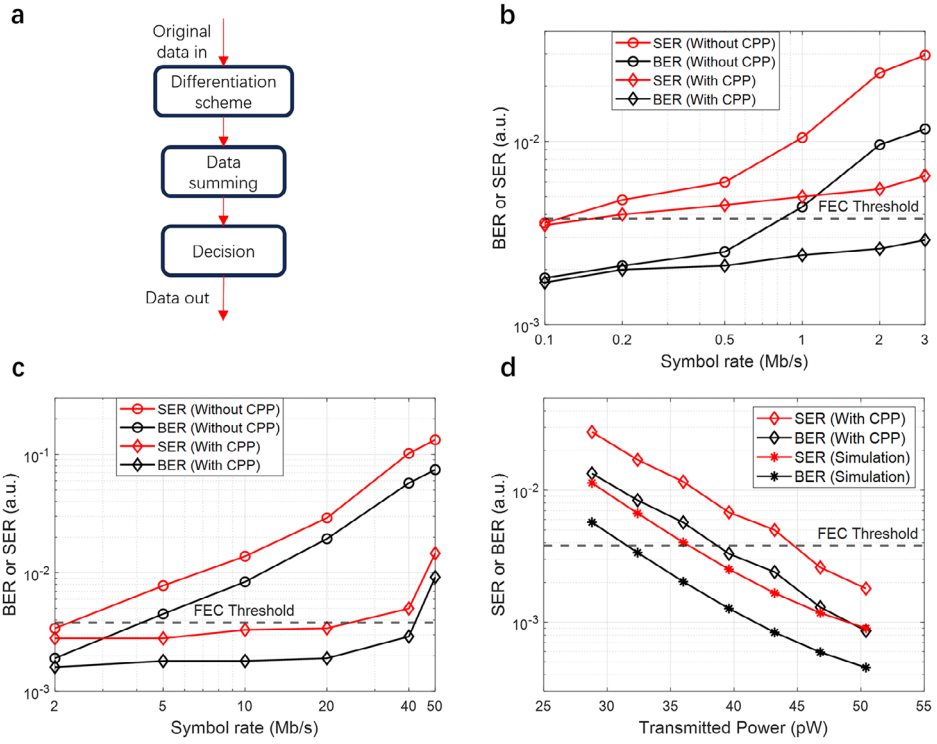

Figure 5. PPM links performance. a) Block diagram for CPP. b) BER and SER versus symbol rate at 128-PPM links. c) BER and SER versus symbol rate at 8-PPM links. d) BER and SER versus transmitted power at 1 Mb s^{-1} 128-PPM links with CPP.

Table 2. Performance of the state-of-the-art UV-C OWC demonstrations.

Year	Operating wavelength	Transmitter	Receiver	Data rate	Received power	BER
2021[33]	276.8 nm	100 μm UV-C micro-LED	Hamamatsu APD C5658	2 Gbit s^{-1}	25 μW	2.86×10^{-3}
2022[30]	285 nm	40 μm UV-C micro-LED	Hamamatsu APD C5668	4.17 Gbit s^{-1}	100 μW	1.12×10^{-4}
2023[27]	273 nm	40 μm UV-C micro-LED	Hamamatsu APD C5668	5.56 Gbit s^{-1}	148 μW	3.8×10^{-3}
2023[5]	275 nm	Thorlabs LED275J	Cooled Hamamatsu S13360-2226	1 Mbit s^{-1}	30 pW	2.4×10^{-3}
2024[6]	276 nm	100 μm UV-C micro-LED	Cooled Hamamatsu S13360-1350 SPL	10 Mbit s^{-1}	220 pW	3.0×10^{-3}
This work	276 nm	100 μm UV-C micro-LED	Cooled Hamamatsu S13360-1350 SPL	120 Mbit s^{-1}	1.728 nW	2.9×10^{-3}

are shown in Figure 5b,c. The result shows that, at 128-PPM links without using CPP, the BER increases from 1.8×10^{-3} to 1.17×10^{-2} and the SER increases from 3.6×10^{-3} to 2.96×10^{-2} with the symbol rate ranging from 100 kb s^{-1} to 3 Mb s^{-1}. At 8 PPM links without using CPP, the BER increases from 1.9×10^{-3} to 7.43×10^{-2} and the SER increases from 3.4×10^{-3} to 1.33×10^{-1} with the symbol rate ranging from 2 to 50 Mb s^{-1}. Both SER and BER increase with the symbol rate because of the ISI.[45] There are two factors contributing to the ISI: the long fall time of received pulses and afterpulses. The long fall time of received pulses can extend into the detection window of the subsequent symbol. Afterpulses are delayed pulses following photon pulses and dark pulses. This is because the carriers may be trapped by the SiPM's lattice defects during the avalanche multiplication. These trapped carriers are released later and multiplied by the avalanche multiplication process to create afterpulses. Afterpulses are the same shape as pulses caused by detected photons and dark counts. Thus, the following symbols can be occupied by afterpulses, causing ISI.

The CPP mitigates the effect of ISI by differentiation, so both SER and BER are reduced. For 128-PPM links, when the symbol rate is 2 Mb s^{-1}, the detection time slot is 62.5 ns, which is larger than the dead time of a pixel (45 ns). Thus, there is no ISI and the BER without CPP is measured at 1.9×10^{-3}. When the symbol rate is 20 Mb s^{-1}, the detection time slot is 6.25 ns, which is much smaller than the dead time of a pixel. Thus, the ISI occurs and the BER without CPP increases to 1.94×10^{-2}. Thanks to the CPP, ISI free is achieved and the BER is reduced to 1.9×10^{-3} at 20 Mb s^{-1} 8-PPM link. The maximum symbol rate of 128-PPM links is 3 Mb s^{-1} with a BER of 2.9×10^{-3}, lower than the FEC threshold. Due to the bandwidth limitation of the transmitter, the symbol rate cannot be further increased because the detection windows will be larger than the time slot. A symbol rate of 40 Mb s^{-1} is achieved at 8-PPM links with a BER of 2.9×10^{-3}, corresponding to a maximum bit rate of 120 Mbit s^{-1}. Moreover, it can be seen that the curves for SER with CPP and BER without CPP cross at a rate of around 1 Mb s^{-1} in Figure 5b whereas this is 3 Mb s^{-1} in Figure 5c. This difference in performance is dependent on the duration of the detection timeslot. This is 7.8 ns for 1 Mb s^{-1} 128-PPM links, and 40 ns for 3 Mb s^{-1} 8 PPM links. Thus, the effect of ISI at 1 Mb s^{-1} 128-PPM links is larger, contributing to a higher BER without CPP. For the curves with CPP, the ISI is mitigated, leading to better performance.

Figure 5d shows the BER and SER versus transmitted power in 1 Mb s^{-1} 128 PPM links. The result shows both BER and SER decrease with the increase in transmitted power, because of the reduction of the probability of symbols without detected photons based on Poisson distribution. Assuming the optimal power corresponds to a BER equal to the FEC threshold, according to Figure 5d, the optimal transmitted power is 38.85 pW. This corresponds to 7.7 transmitted photons per bit or 6.1 detected photons per symbol for 1 Mb s^{-1} 128-PPM links. To achieve the quantum limit of 5 detected photons per symbol, to achieve the quantum limit of 5 detected photons per symbol, the SiPM's temperature or active area should be further reduced to minimize the DCR, while advancements in manufacturing technology are needed to mitigate the impact of afterpulses. Additionally, simulation results are added to Figure 5d to compare with the experimental result. The detailed theoretical analysis of SER and BER is shown in Note S3 (Supporting Information). The simulation result performs better than the experimental result in terms of SER and BER. This is because the simulation does not consider ISI, due to the long fall time and afterpulses. Typically, an additional 7–10 pW of power is required to compensate for the effects of ISI at 1 Mb s^{-1} for 128-PPM links, in order to achieve a similar BER and SER. To further investigate the impact of long fall time and afterpulses, the simulated and experimental results for 128-PPM links at 1 Mb s^{-1} and 0.1 Mb s^{-1} are compared. Both of the long fall time and afterpulses contribute to ISI at 1 Mb s^{-1}, whereas only afterpulses contribute at 0.1 Mb s^{-1} (as the detection window is longer than the pulse duration). The simulated BER is calculated as 8.4×10^{-4} for both symbol rates. The experimental BER is 2.4×10^{-3} and 1.7×10^{-3} at 1 and 0.1 Mb s^{-1} respectively. Thus, the difference in BER between experiment and simulation is reduced from 1.56×10^{-3} to 8.6×10^{-4}. This reduction occurs because the effect of long fall time is eliminated, leaving afterpulses as the source of the remaining difference. The change in SER follows a similar trend to that of the BER.

The performance of state-of-the-art UV-C OWC demonstrations is summarized in **Table 2**. A maximum data rate of 5.56 Gbit s^{-1} was reported in ref. [27], but the received power exceeded 100 μW. In contrast, this work demonstrated a 120 Mbit/s link with a

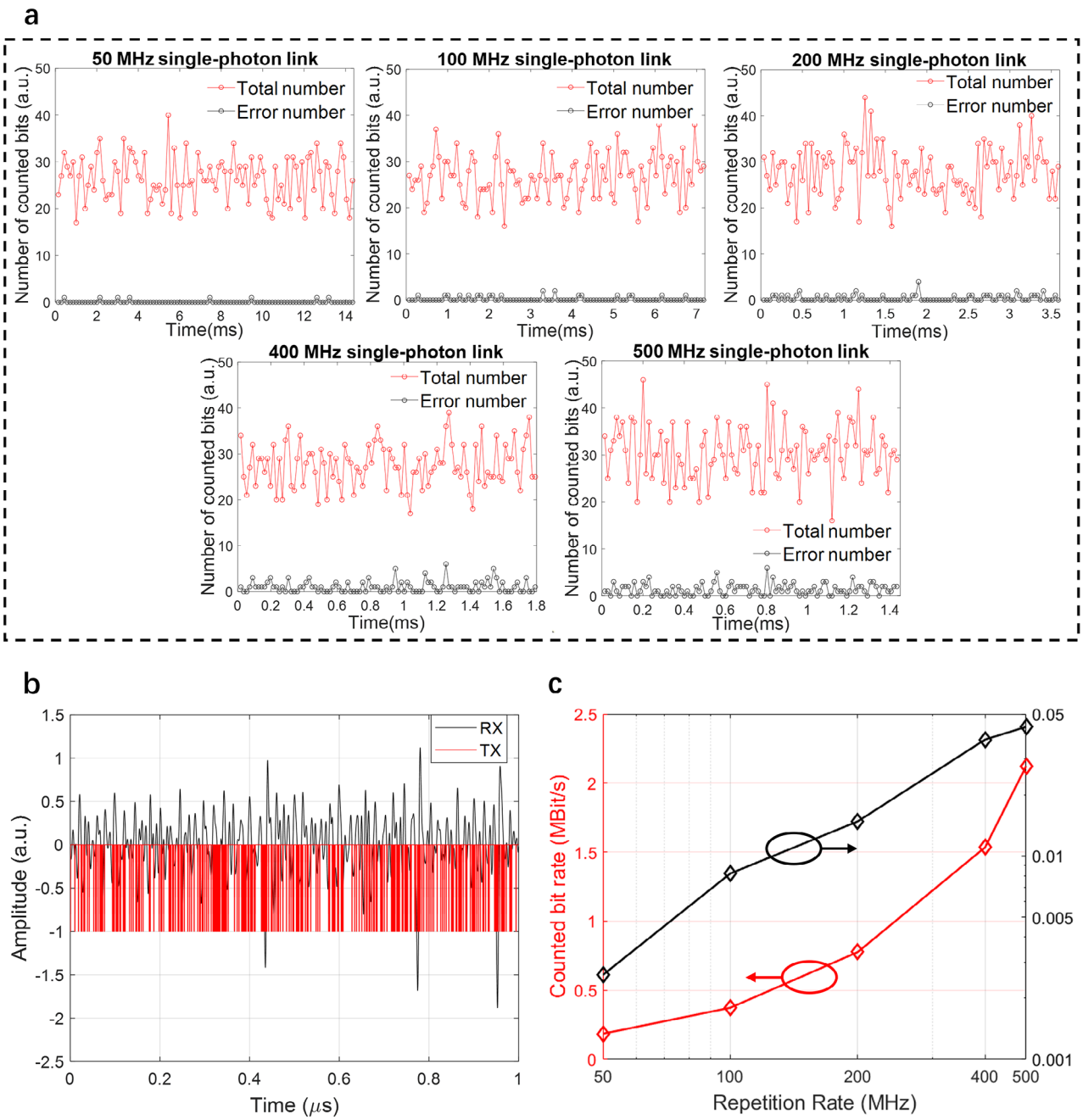

Figure 6. Single-photon links performance. a) Number of total counted bits and error bits versus time under repetition rate from 50 to 500 MHz. b) Transmitted sequence and synchronized received pulses at 500 MHz repetition rate. c) Counted bit rate and BER versus repetition rate.

received power of 1.728 nW because of the high sensitivity of our UV-C SPD.

2.6. Single-Photon Link Performance

In addition to conventional communications, the micro-LEDs and SiPM also have the potential for establishing QKD links.[46–48] Thus, single-photon links were built to verify our UV-C SPD's single-photon counting capability and its suitability for QKD. In a BB84 QKD, four light sources and four detectors are required for generating and receiving four different polarized quantum bits (qubits). Because polarization is randomly chosen in the transmitter and each detector receives qubits with one specific polarization, only one-fourth of the total qubits are collected by each detector. For the single-photon links in this paper, "1" and "0" are randomly selected to activate and deactivate the micro-LED respectively and only detected bits "1" are counted by the UV-C SPD. Consequently, this is equivalent to half of the total qubits being collected by one detector. With the use of the

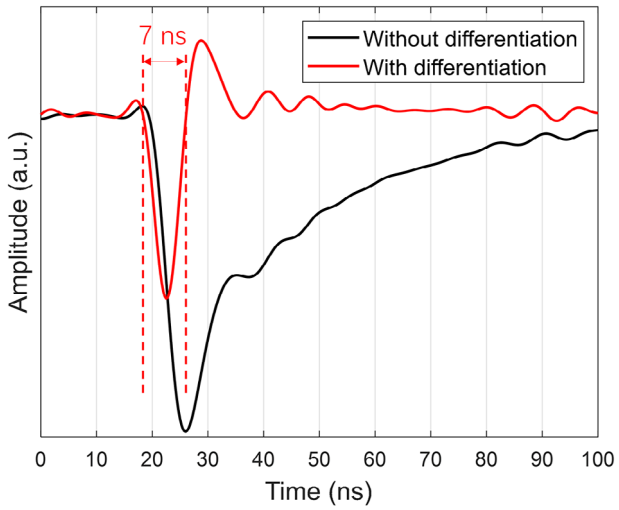

Figure 7. A received pulse with and without differentiation.

UV-C SPD in a BB84 QKD system, the error number is unchanged, and the counted qubits number becomes half for each SPD compared to the single-photon link in this paper, resulting in the BER double. According to a quantum BER (QBER) threshold of 1.1×10^{-1} for QKD systems,[49] a BER of less than 5.5×10^{-2} in single-photon links can indicate the potential for establishing a QKD system.

For single-photon link demonstration, in the transmitter, a PRBS sequence was generated and modulated the micro-LED with an OOK signal. The pulse width was set as 2 ns and the repetition rate ranging from 50 MHz to 500 MHz was used. Then, the OOK signal was attenuated to a single-photon level (0.07 transmitted photon per "1" bit) and emitted out from the transmitter. In the receiver, the CPP was also used to mitigate the ISI. The detection window was fixed at 2 ns and the synchronization was achieved by correlation. According to **Figure 6b**, the peak amplitude of different single pulses after differentiation varies but is always below an absolute value of "−1.25". Based on the number of 8 sampling points due to a 4 GS s^{-1} sampling rate within each detection window, the decision threshold was set as "−10". If the summed value within the detection window is less than the threshold, the bit is decided as "1," otherwise decided as "0". The counted bits refer to the transmitted bits "1" correctly detected as "1" and the counted bit rate is defined as the counted bits number divided by time duration. Then, compared with the transmitted PRBS sequences, the error bits are counted if the bit in the received sequence is "1" while "0" in the corresponding transmitted PRBS sequences. The BER is defined as the error bits number divided by the counted bits number.

Figure 6a shows the counted bits number and error bits number versus time with a repetition rate from 50 MHz to 500 MHz. The value of each point was obtained by transmitting 7×2^{10} bits. The results show that the value of the counted bits number fluctuates around 30, but the error bits number increases with the repetition rate because of the ISI. Figure 6b illustrates the synchronized received pulses and the corresponding transmitted PRBS sequence during 1 μs with the repetition rate of 500 MHz. The values "−1" and "0" in the red line represent "1" and "0" in the transmitted sequences, respectively. Most of the transmitted "1" bits are detected as "0" because the average detected photon number per "1" bit is very low, approximately $0.07 \times 0.924 \times 0.83 \times 0.1476 \approx 0.008$. The calculated BER and counted bit rate versus repetition rate are plotted in Figure 6c. The BER increases from 2.6×10^{-3} to 4.32×10^{-2}, which is always below the threshold of 5.5×10^{-2}, with a repetition rate ranging from 50 to 500 MHz. Moreover, the maximum counted bit rate achieves 2.12 Mbit s^{-1}. The repetition rate cannot be further increased because the detection windows will be larger than each bit's time interval.

3. Conclusion

In conclusion, this paper presents ultralow photon flux OWC links using a 100 μm diameter UV-C micro-LED and a SiPM-based UV-C SPD. Unlike previously reported UV SPDs,[15–18] a design based on commercial devices is one advantage of our UV-C SPD. Cooling is clearly advantageous, enhancing the UV-C SPD's sensitivity by lowering the SiPM temperature to -20 °C, which in turn reduces the DCR to 2.1 kcps. The cooling technique will also improve SPD performance at other wavelengths. A minimum transmitted photon number per bit of 7.7 (corresponding to 0.97 detected photon per bit) was demonstrated in 1 Mb s^{-1} 128-PPM links, which is the first reported Mbit s^{-1}-level UV-C wireless communication link operating with less <10 transmitted photons per bit and <1 detected photon per bit. Additionally, the maximum data rate of the PPM link achieved 120 Mbit s^{-1} at 40 Mb s^{-1} 8-PPM links. Compared with the recently reported result,[5] the average photon number per bit reduces by 82% and the data rate increases by 120 times. These benefit from the higher sensitivity of the UV-C SPD and the higher modulation bandwidth of the UV-C micro-LED. Moreover, the transmitted irradiance of all demonstrated PPM links successfully satisfies eye and skin safety standards, while previous UV-C communication demonstrations, to the best of our knowledge,

Table 3. Different performance based on using the matched filter or/and differentiation.

Option	Definition of matched filter	SER	BER
Only differentiation	N/A	0.0050	0.0029
Only matched filter	Fitting pulse in Figure 3e	0.1130	0.0627
Matched filter followed by the differentiation	Pulse after differentiation in Figure 7	0.2595	0.1316
Differentiation followed by the matched filter	Pulse after differentiation in Figure 7	0.0298	0.0182

do not meet this constraint.[30,33] Such PPM links could provide low-energy consumption communication services in a range of applications.[50] Furthermore, a 500 MHz repetition rate single-photon link was demonstrated, resulting in a BER of 4.32×10^{-2} and a counted bit rate of 2.12 Mbit s^{-1}. This is the first single-photon link demonstrated in the UV-C region, indicating a UV-C QKD system operating with a secure key rate (SKR) of Mbit s^{-1}-level.

The main noise source of the UV-C SPD is dark counts, and the corresponding theoretical analysis is shown in Note S3 (Supporting Information). Further reducing the temperature and active area of the SiPM can achieve a lower DCR. Additionally, whilst the current links work in a "solar-blind" region of the daylight spectrum and benefit from the very low levels of ambient light, the UV-C SPD is sensitive to the much stronger daylight in the visible and near IR regions. Future work will focus on developing filtering strategies that will enable daylight operation.

4. Experimental Section

Micro-LED Design and Manufacture: The UV-C micro-LED used in this work were fabricated from commercially available AlGaN-based LED wafers grown on 2″ c-plane sapphire substrate with the designed central emission wavelength of 280 nm. The epitaxial structure of this wafer is similar to the one reported in our previous work,[51] including a 2 µm thick AlN buffer layer, a 2 µm thick n-doped $Al_{0.6}Ga_{0.4}N$ layer, an active region consisting of six-period AlGaN-based quantum wells with a 2.5 nm thick well and 13 nm thick barrier, a 50 nm thick $Al_{0.6}Ga_{0.4}N$ electron blocking layer, and finally a 310 nm thick p-doped GaN layer. The Al compositions in the wells and barriers are estimated as 45% and 55%, respectively. The detailed fabrication process of the different-size LEDs with flip-chip configuration is as follows: circular LEDs with different diameters from 100 µm to 300 µm were created through the standard UV photolithography and Cl2-based inductively coupled plasma etching techniques. Then the high-temperature annealed Ti/Al/Ti/Au and as-deposited Pd were employed as the ohmic contact to n-type AlGaN and p-type GaN. A SiO_2 passivation layer was further deposited to isolate each LED. After selectively removing SiO_2 from the designed area, the Ti/Au tracks were deposited to simplify individual-anode addressing of each LED with a shared cathode. The fabricated LEDs were wire-bonded to a printed circuit board without thermal management for further characterization and OWC measurement.

The bandwidth of the AlGaN-based UV-C micro-LED increases with the decrease in size, which has been investigated in previous research.[27] The function of the micro-LED in this work is to provide high-speed modulated signals, so the micro-LED with the smallest diameter available, 100 µm, was chosen.

PCB Design: The amplitude of a single pulse generated by the SiPM is insufficient to be measured by a commercial oscilloscope without external amplification. The PCB is designed to both supply bias voltage to the SiPM and amplify the pulses generated by the SiPM. The bias voltage is provided by a power supply module (HAMAMATSU C11204-01) integrated into the PCB board. The power supply module is remotely controlled using serial communication, adjusting the bias voltage between 20 V and 90 V. The pulses are amplified by an 8 GHz gain bandwidth product (GBWP) transimpedance amplifier (TIA, Texas OPA855-Q1). The theoretical 3-dB bandwidth of the amplifier can be calculated by:[52]

$$f_{3dB} \approx \sqrt{\frac{GBWP}{2\pi R_F C_{in}}} \tag{5}$$

where R_F is the resistance of the transimpedance load and C_{in} is the input capacitance of the TIA. The resistance of the transimpedance load is 1500 Ω and the input capacitance is dominated by the SiPM's capacitance of approximately 60 pF. Thus, the theoretical 3 dB bandwidth of the amplifier is calculated as 120 MHz. The measured practical bandwidth (110 MHz) is slightly smaller than the theoretical bandwidth, probably due to the additional parasitic capacitance on the PCB board. The electrical noise from the amplifier does not affect the pulse shape, as it is at too low a level. This can be seen in Figure 3e, showing that the single pulse can clearly be distinguished from the noise floor.

Differentiation Scheme in CPP: Previous research has proven a differentiation detection scheme can efficiently mitigate the ISI caused by the long fall time of pulses.[43,53] **Figure 7** shows a received pulse with and without differentiation. The time duration of the pulse is reduced to approximately 7 ns with differentiation. The effect of the positive peak following the negative peak is negligible because only the points within the detection windows are the key to the symbol decision. In this paper, the differentiation scheme is achieved by taking the first order derivate of the received pulse. Higher differentiation orders have been tried, which have not been adopted because of worse performance.[53]

The matched filter is another method against the ISI in ultralow photon flux PPM links.[37] However, the matched filter does not work well in our work. Based on using the matched filter or/and differentiation, there are four options: only differentiation, only matched filter, matched filter followed by the differentiation and differentiation followed by the matched filter. The definition of the matched filter and the corresponding SER and BER from 40 Mb s^{-1} 8-PPM links are shown in **Table 3**. The result shows using only differentiation achieves the best SER and BER performance. This is because the shape of received pulses is changing due to the random overlap of multiple single pulses within 2 ns in each symbol. Thus, an optimal matched filter does not exist.

Supporting Information

Supporting Information is available from the Wiley Online Library or from the author.

Acknowledgements

The authors thank the support from Andy Schreier (Fraunhofer Institute for Telecommunications, Germany), Abderrahmen Trichili (University of Oxford, UK), Vincent Lee (University of Oxford, UK) and Hyunchae Chun (Incheon National University, South Korea). The research on micro-LED was supported by the TITAN Hub (EPSRC grant EP/Y037243/1).

Conflict of Interest

The authors declare no conflict of interest.

Author Contributions

F.L. and D.O'B. developed the research concepts. J.J.D.M., E.X., J.H., J.H., and M.D.D. designed and manufactured the micro-LED. F.L., J.F., G.F., and Q.Z. designed and built the UV-C SPD. F.L. set up the communication links, collected the data and finished the post-processing with substantial contributions from J.F., Z.W., and J.W. F.L. wrote the first draft of the manuscript, revised by D.O'B. All the authors reviewed the paper and contributed to the final manuscript.

Data Availability Statement

Data underlying the results presented in this paper are not publicly available but may be obtained from the authors upon reasonable request.

Keywords

micro-LED, optical wireless communications, silicon photomultiplier (SiPM), single-photon detector, ultralow photon flux, UV-C

Received: October 27, 2024
Revised: March 12, 2025
Published online:

[1] Z. Ghassemlooy, S. Arnon, M. Uysal, Z. Xu, J. Cheng, *IEEE J. Sel. Areas Commun.* **2015**, *33*, 1738.
[2] D. O. Brien, R. Turnbull, H. L. Minh, G. Faulkner, O. Bouchet, P. Porcon, M. E. Tabach, E. Gueutier, M. Wolf, L. Grobe, J. Li, *J. Lightwave Technol.* **2012**, *30*, 2181.
[3] A. Schreier, O. Alia, R. Wang, R. Singh, G. Faulkner, G. Kanellos, R. Nejabati, D. Simeonidou, J. Rarity, D. O. Brien, *J. Lightwave Technol.* **2023**, *41*, 5226.
[4] H. Huang, G. Xie, Y. Yan, N. Ahmed, Y. Ren, Y. Yue, D. Rogawski, M. J. Willner, B. I. Erkmen, K. M. Birnbaum, S. J. Dolinar, M. P. J. Lavery, M. J. Padgett, M. Tur, A. E. Willner, *Opt. Lett.* **2014**, *39*, 197.
[5] F. Liu, J. Farmer, A. Schreier, G. Faulkner, H. Chun, W. Matthews, Z. Wang, D. O'Brien, *Opt. Lett.* **2023**, *48*, 5387.
[6] F. Liu, J. Farmer, G. Faulkner, Z. Wang, J. Wang, D. O. Brien, E. Xie, J. Hill, J. Herrnsdorf, J. J. D. McKendry, M. D. Dawson, in *2024 Conf. on Lasers and Electro-Optics (CLEO,* Eds: *D. Venkitesh)*, Optica Publishing Group, Washington, DC **2024**, 1.
[7] C. H. Bennett, G. Brassard, *Theor. Comput. Sci.* **2014**, *560*, 7.
[8] W. Li, L. Zhang, H. Tan, Y. Lu, S.-K. Liao, J. Huang, H. Li, Z. Wang, H.-K. Mao, B. Yan, Q. Li, Y. Liu, Q. Zhang, C.-Z. Peng, L. You, F. Xu, J.-W. Pan, *Nat. Photonics* **2023**, *17*, 416.
[9] H. Chun, I. Choi, G. Faulkner, L. Clarke, B. Barber, G. George, C. Capon, A. Niskanen, J. Wabnig, D. O'Brien, D. Bitauld, *Opt. Express* **2017**, *25*, 6784.
[10] V. Lee, D. O'Brien, in *2020 IEEE Photonics Conf. (IPC,* Eds: *G. Bosco)*, IEEE, Piscataway, NJ **2020**, pp. 1–2.
[11] NREL, Reference Air Mass 1.5 Spectra, https://www.nrel.gov/grid/solar-resource/spectra-am1.5.html, (accessed: March, 2025).
[12] E. C. f. E. Standardization, BS EN 62471: Photobiological safety of lamps and lamp systems, http://tbt.testrust.com/image/zt/123/100123_2.pdf, (accessed: March, 2025).
[13] R. H. Hadfield, *Nat. Photonics* **2009**, *3*, 696.
[14] F. Ceccarelli, G. Acconcia, A. Gulinatti, M. Ghioni, I. Rech, R. Osellame, *Adv. Quantum Technol.* **2021**, *4*, 2000102.
[15] E. E. Wollman, V. B. Verma, A. D. Beyer, R. M. Briggs, B. Korzh, J. P. Allmaras, F. Marsili, A. E. Lita, R. P. Mirin, S. W. Nam, M. D. Shaw, *Opt. Express* **2017**, *25*, 26792.
[16] L. Su, D. Zhou, H. Lu, R. Zhang, Y. Zheng, *J. Semicond.* **2019**, *40*, 121802.
[17] L. Li, D. Zhou, F. Liu, H. Lu, F. Ren, D. Chen, R. Zhang, Y. Zheng, *IEEE Photonics Technol. Lett.* **2016**, *28*, 2526.
[18] E. Cicek, Z. Vashaei, R. McClintock, C. Bayram, M. Razeghi, *Appl. Phys. Lett.* **2010**, *96*, 261107.
[19] A. N. Otte, D. Garcia, T. Nguyen, D. Purushotham, *Nucl. Instrum. Methods Phys. Res., Sect. A* **2017**, *846*, 106.
[20] W. Ali, R. Chen, M. Crisp, R. V. Penty, *J. Lightwave Technol.* **2023**, *42*, 1375.
[21] W. Matthews, Z. Ahmed, W. Ali, S. Collins, *IEEE Photonics Technol. Lett.* **2021**, *33*, 487.
[22] J. Riu, M. Sicard, S. Royo, A. Comerón, *Opt. Lett.* **2012**, *37*, 1229.
[23] G. Gariepy, N. Krstajić, R. Henderson, C. Li, R. R. Thomson, G. S. Buller, B. Heshmat, R. Raskar, J. Leach, D. Faccio, *Nat. Commun.* **2015**, *6*, 6021.
[24] P. Tian, X. Shan, S. Zhu, E. Xie, J. J. D. McKendry, E. Gu, M. D. Dawson, *IEEE J. Quantum Electron.* **2022**, *58*, 3300214.
[25] T. Lu, X. Lin, W. Guo, C.-C. Tu, S. Liu, C.-J. Lin, Z. Chen, H.-C. Kuo, T. Wu, *Opto-Electron. Sci.* **2022**, *1*, 220020.
[26] J. J. D. McKendry, E. Xie, J. Hill, H. Zimi, J. Herrnsdorf, E. Gu, R. K. Henderson, M. D. Dawson, *IEEE Photonics J.* **2023**, *15*, 8200806.
[27] J. Hill, C. Chen, E. Xie, J. J. D. McKendry, J. Herrnsdorf, E. Gu, H. Haas, M. D. Dawson, *IEEE Photon. J.* **2023**, *15*, 7305108.
[28] Z. Rao, X. Shan, G. Wang, Z. Jin, R. Lin, X. Cui, R. Liu, K. Xu, P. Tian, *J. Lightwave Technol.* **2024**, *42*, 4360.
[29] P. J. Parbrook, B. Corbett, J. Han, T.-Y. Seong, H. Amano, *Laser Photonics Rev.* **2021**, *15*, 2000133.
[30] D. M. Maclure, J. J. D. McKendry, M. S. Islim, E. Xie, C. Chen, X. Sun, X. Liang, X. Huang, H. Abumarshoud, J. Herrnsdorf, E. Gu, H. Haas, M. D. Dawson, *Photonics Res.* **2022**, *10*, 516.
[31] H. X. Jiang, J. Y. Lin, *Opt. Express* **2013**, *21*, A475.
[32] A. R. Anwar, M. T. Sajjad, M. A. Johar, C. A. Hernández-Gutiérrez, M. Usman, S. P. Łepkowski, *Laser Photonics Rev.* **2022**, *16*, 2100427.
[33] S. Zhu, P. Qiu, Z. Qian, X. Shan, Z. Wang, K. Jiang, X. Sun, X. Cui, G. Zhang, D. Li, P. Tian, *Opt. Lett.* **2021**, *46*, 2147.
[34] D. M. Maclure, C. Chen, J. J. D. McKendry, E. Xie, J. Hill, J. Herrnsdorf, E. Gu, H. Haas, M. D. Dawson, *Opt. Express* **2022**, *30*, 46811.
[35] H. Yu, S. Xiao, M. H. Memon, Y. Luo, R. Wang, D. Li, C. Shen, H. Sun, *Laser Photonics Rev.* **2024**, *18*, 2300789.
[36] HAMAMATSU, MPPC S13360 series, https://www.hamamatsu.com/jp/en/product/optical-sensors/mppc/mppc_mppc-array.html, (accessed: October, 2024).
[37] H. Hao, Q.-Y. Zhao, Y.-H. Huang, J. Deng, F. Yang, S.-Y. Ru, Z. Liu, C. Wan, H. Liu, Z.-J. Li, H.-B. Wang, X.-C. Tu, L.-B. Zhang, X.-Q. Jia, X.-L. Wu, J. Chen, L. Kang, P.-H. Wu, *Light: Sci. Appl.* **2024**, *13*, 25.
[38] H. Kaushal, G. Kaddoum, *IEEE Commun. Surv. Tutorials* **2017**, *19*, 57.
[39] Z. Zeng, S. Fu, H. Zhang, Y. Dong, J. Cheng, *IEEE Commun. Surv. Tutorials* **2017**, *19*, 204.
[40] A. Elfikky, A. I. Boghdady, S. Mumtaz, E. E. Elsayed, M. Singh, S. A. Abd El-Mottaleb, S. A. H. Mohsan, M. H. Aly, *Opt. Quantum Electron.* **2024**, *56*, 1617.
[41] E. E. Elsayed, *Opt. Commun.* **2024**, *562*, 130558.
[42] E. E. Elsayed, M. R. Hayal, I. Nurhidayat, M. A. Shah, A. Elfikky, A. I. Boghdady, D. A. Juraev, M. A. Morsy, *IET Optoelectron.* **2024**, *18*, 11.
[43] M. C. Gursoy, M. Nasiri-Kenari, U. Mitra, *Digital Signal Process.* **2022**, *124*, 103161.
[44] D. Hall, Y. H. Liu, L. Yan, Y. Yu, Y. H. Lo, *IEEE Trans. Electron Devices* **2017**, *64*, 4812.
[45] W. Matthews, W. Ali, Z. Ahmed, G. Faulkner, S. Collins, *IEEE Photonics Technol. Lett.* **2021**, *33*, 449.
[46] E. Zhang, F. Liu, *Proc. SPIE* **2024**, *13496*, 134961E.
[47] J. Aldama, S. Sarmiento, I. H. L. Grande, S. Signorini, L. T. Vidarte, V. Pruneri, *J. Lightwave Technol.* **2022**, *40*, 7498.
[48] D. Lowndes, S. Frick, B. Harrington, J. Rarity, in *2017 European Conf. on Lasers and Electro-Optics - European Quantum Electronics Conf.*, (Eds: G. Weihs), Optica Publishing Group, Washington, DC, **2017**, 1.
[49] R. Y. Q. Cai, V. Scarani, *New J. Phys.* **2009**, *11*, 045024.
[50] L. Feng, R. Q. Hu, J. Wang, P. Xu, Y. Qian, *IEEE Network* **2016**, *30*, 77.
[51] X. He, E. Xie, M. S. Islim, A. A. Purwita, J. J. D. McKendry, E. Gu, H. Haas, M. D. Dawson, *Photonics Res.* **2019**, *7*, B41.
[52] P. Horowitz, W. Hill, *The Art of Electronics*, Cambridge University Press, Cambridge **2015**.
[53] M. C. Gursoy, U. Mitra, in *GLOBECOM 2020 - 2020 IEEE Global Communications Conf.*, (Eds: L.-C. Wang) IEEE, Piscataway, NJ **2020**, pp. 1–6.